Master's thesis
Your Field

Formation of cores by merging supermassive black holes

Joonas Suortti

July 16, 2019

Tutor: prof. Smith

Censors: prof. Smith
doc. Smythe

UNIVERSITY OF HELSINKI
DEPARTMENT OF SOMETHING

PL 42 (Kuvitteellinen katu 1)
00014 Helsingin yliopisto

"Bachelor's degrees make pretty good placemats if you get them laminated."

—Jeph Jacques

HELSINGIN YLIOPISTO — HELSINGFORS UNIVERSITET — UNIVERSITY OF HELSINKI

Tiedekunta — Fakultet — Faculty		Laitos — Institution — Department	
Faculty of Whatever		Department of Something	
Tekijä — Författare — Author			
Joonas Suortti			
Työn nimi — Arbetets titel — Title			
Formation of cores by merging supermassive black holes			
Oppiaine — Läroämne — Subject			
Your Field			
Työn laji — Arbetets art — Level	Aika — Datum — Month and year		Sivumäärä — Sidoantal — Number of pages
Master's thesis	July 16, 2019		0 pages

Tiivistelmä — Referat — Abstract

Abstract goes here.

Avainsanat — Nyckelord — Keywords

Your keywords here

Säilytyspaikka — Förvaringsställe — Where deposited

Muita tietoja — övriga uppgifter — Additional information

Contents

1. Introduction

2. Theory

3. KETJU

4. Merger Simulations Using KETJU

We analyse the results of two sets of galaxy merger simulations, where the merger progenitor galaxies contain central supermassive black holes. The simulation are done using the KETJU code by Mannerkoski et al. (2019) and Rantala et al. (2018). The reasoning behind this analysis is to determine if merging SMBHs are able to cause the formation of cored galaxies, how the black hole masses affect the size of the core, and if the KETJU-code produces merger remnants comparable to observations.

4.1   Simulation Details

All of the analysed simulation runs use merger progenitor galaxies from the same progenitor pool. There are seven different progenitors in total. Six of them (BH-1 - BH-6) contain central supermassive black holes, with the SMBH masses varying from $8.5 \times 10^8 M_\odot$ to $8.5 \times 10^9 M_\odot$. The seventh progenitor (BH-0) doesn't contain an SMBH in its centre, and is included simply for the sake of comparison. The detailed masses of the progenitors' central SMBHs are listed in table 4.1.

Apart from the SMBH masses however, all of the progenitor galaxies have identical physical properties. These properties, which are motivated by observations and dynamical simulations of NGC 1600 (Rantala et al., 2018), are described in table 4.2.

Progenitor	$M_\bullet \ [\times 10^9 M_\odot]$
BH-0	-
BH-1	0.85
BH-2	1.7
BH-3	3.4
BH-4	5.1
BH-5	6.8
BH-6	8.5

Table 4.1: Central SMBH masses of the progenitors used in the analysed simulations.

Alongside the physical properties, the distributions of the different particles that make up the progenitor galaxies are also identical. While the central SMBHs are simply modelled as point masses in a progenitor's internal coordinate system, the stellar and dark matter particles are distributed according to a Dehnen density-potential model (Dehnen, 1993):

$$\rho(r) = \frac{(3-\gamma)M}{4\pi} \frac{a}{r^\gamma (r+a)^{4-\gamma}}, \tag{4.1}$$

$$\phi(r) = \frac{GM}{a} \times \begin{cases} -\frac{1}{2-\gamma}\left[1 - \left(\frac{r}{r+a}\right)^{2-\gamma}\right] & \gamma \neq 2 \\ \ln\frac{r}{r+a} & \gamma = 2 \end{cases}, \tag{4.2}$$

where M is the total mass, a is a scaling radius, and γ is the central slope of the profile. The fundamental difference between the models describing the distributions of the two particle types is that, for stellar particles the value used for γ is 3/2, while for the dark matter particles $\gamma = 1$.

While the merger progenitor galaxies are the same, the initial conditions of the simulations are quite different. The Mannerkoski et al. (2019) simulations comprise of four subsequent runs where the progenitor galaxy BH-6 (table 4.1) is merged with

$M_\star$	R_e	M_{DM}	$f_{\mathrm{DM}}(r_{1/2})$	$N_\star$	N_{DM}
$[\times 10^{11} M_\odot]$	[kpc]	$[\times 10^{13} M_\odot]$			
4.15	7	7.5	0.25	4.15×10^6	1.0×10^7

Table 4.2: The physical properties, constant throughout the different progenitor galaxies:

$M_\star$: Stellar mass

R_e: Effective radius

M_{DM}: Mass of the dark matter halo

$f_{\mathrm{DM}}(r_{1/2})$: Fraction of dark matter mass compared to stellar mass inside the effective radius

$N_\star$: Number of stellar particles

N_{DM}: Number of dark matter particles

the progenitor BH-2. On the other hand, the simulations done by Rantala et al. (2018) contain simply seven different mergers between two of the same progenitor galaxies.

The results gathered from the two sets of simulations also differ from each other. From the simulations done by Mannerkoski et al. (2019); only the locations, velocities and masses of the central SMBHs are saved. The data comes from time steps starting from when the semi-major-axis of the merging SMBH binary is $a \lesssim 5000 R_s$ (R_s is the Schwarzschild radius) up until the end of the simulation. The simulation results of Rantala et al. (2018) however consists of not only the properties of the black holes, but also of the stellar and dark matter particles. These results are given in the form of a single snapshot at the simulation time $t = 2\mathrm{Gyr}$. Due to the distinct difference between the type of results gained from the two different simulation sets (and for simplicity's sake), we will, from now on, be calling the simulations from Mannerkoski et al. (2019) "Runs", and the ones from Rantala et al. (2018) "Snapshots" (table 4.3).

Mannerkoski et al. (2019)			Rantala et al. (2018)		
Run	$M_{\bullet,1}[10^9 M_\odot]$	$M_{\bullet,2}[10^9 M_\odot]$	Snapshot	$M_{\bullet,1}[10^9 M_\odot]$	$M_{\bullet,2}[10^9 M_\odot]$
1	8.5	1.7	0	-	-
2	10.2	1.7	1	0.85	0.85
3	11.9	1.7	2	1.7	1.7
4	13.6	1.7	3	3.4	3.4
			4	5.1	5.1
			5	6.8	6.8
			6	8.5	8.5

Table 4.3: Central SMBH masses of the progenitors used in the different simulation runs.

4.2 Black Hole Trajectories

4.3 Core Size Measurements

In order to check if a merger remnant is cored or not, we first have to calculate their surface brightness profiles, and then see if they contain surface brightness deficiencies near the centre of the merger. As the "Runs" don't contain stellar data, we use the "Snapshots" for the core analysis.

We calculate the surface brightness profiles from the snapshots by: changing the coordinate system to centre-of-mass coordinates, projecting the stellar particles onto a plane, and calculating masses inside logarithmically space radial bins to get a radial mass surface density profile. We then do the aforementioned calculations 100 times from random viewing angles and calculate the azimuthal average of the profiles. This allows us to form a smooth mass surface density profile, which we then turn into a surface brightness profile by assuming a mass-to-light ratio of $M/L = 4$ (Rantala et al., 2018).
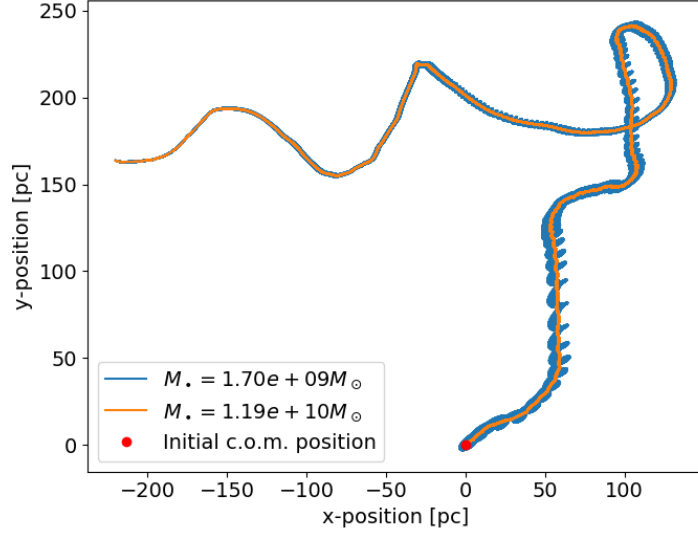
Figure 4.1: The trajectories of the black holes during "run 3" of the simulation. The coordinates are centred on the initial location of the centre-of-mass of the black hole system. The orange and blue lines show the paths taken by the smaller and larger black holes respectively during the simulation. Both paths show clear spiral patterns which become smaller and smaller as the simulation proceeds. The paths end at the location where the black holes merge, i.e. where the distance between them is below the specific threshold.

In figure 4.3, one can see example surface brightness profiles for all of the snapshots. Looking at the different curves, it seems like the presence of central SMBHs in the merger progenitors does cause some kind of brightness deficiency near the galactic centre of the remnant's surface brightness profile. Not only that, the higher the mass of the central black holes, the larger the surface brightness deficiency seems to be.

The deficiencies found in the surface brightness profiles mentioned above imply the presence of cores, however determining the precise size of the core requires us to find the exact location where the deviations from the expected power-law profile start. This can be done by fitting the calculated profile with a model that is a combination of two power laws: a shallow inner power-law, and a steeper outer
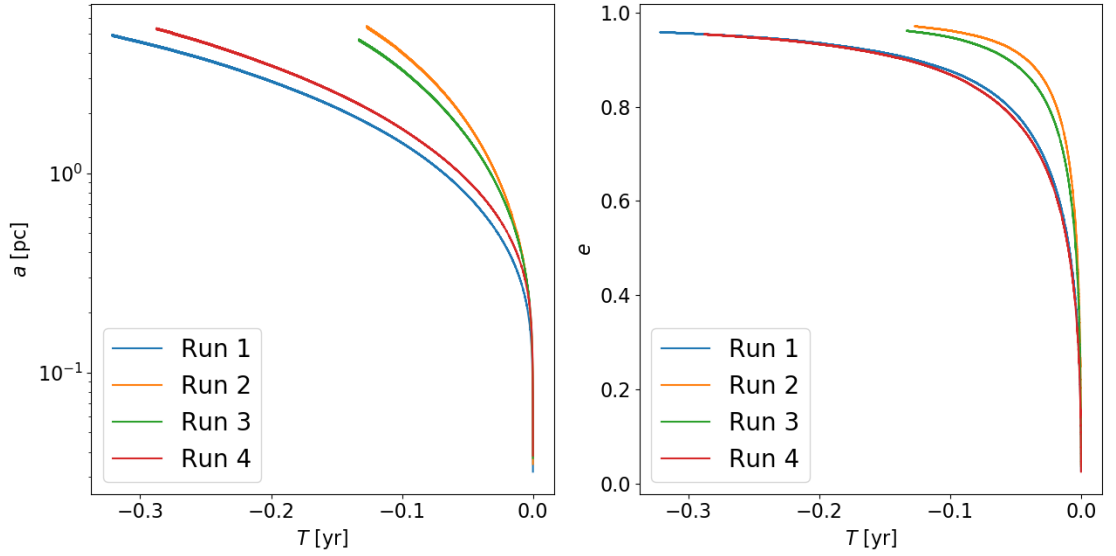
Figure 4.2: The semi-major axes (left) and eccentricities (right) of the black hole systems in simulation runs 1-4 as a function of time. The zero position on the x-axis corresponds to the point of time in the simulation, where the black hole merging event happens.

power-law. The radius at which the power laws shift, i.e. the break radius r_b, is equivalent to the radius of the core.

There are two commonly used options for modelling the surface brightness profiles. The first one is the core-Sérsic profile (Graham et al., 2003a), which can be expressed using the following equation:

$$\mu(r) = \mu' \left[1 + \left(\frac{r_b}{r} \right)^\alpha \right]^{\gamma/\alpha} \exp \left\{ -b_n \left[(r^\alpha + r_b^\alpha) / r_e^\alpha \right]^{1/(\alpha n)} \right\}, \tag{4.3}$$

where r_b is the break radius, γ is the logarithmic slope of the inner power-law, α controls the sharpness of the transition between the two power-laws, r_e and n are the effective half-mass radius and the Sérsic index of the outer power-law, and the normalization factor μ' is defined by:

$$\mu' = \mu_b 2^{-\gamma/\alpha} \exp \left[b_n \left(2^{(}1/\alpha) r_b / r_e \right)^{1/n} \right], \tag{4.4}$$

where μ_b is the surface brightness at the break radius.

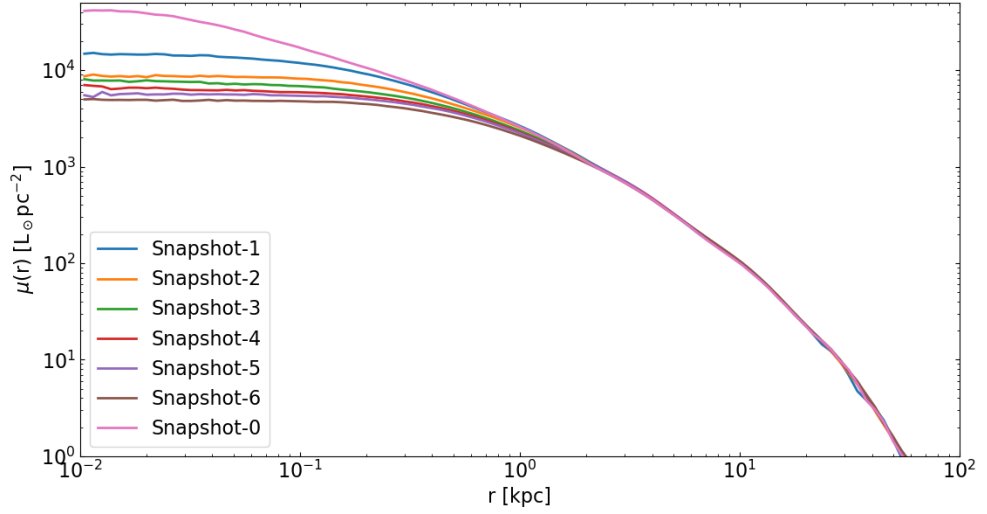The second option for determining the core radius through profile fitting, is

Figure 4.3: Surface brightness profiles of all of the simulated merger remnants. The profiles were calculated by dividing the remnants into 100 radial bins, and averaging the surface brightness inside the bins through 100 random viewing angles. The luminosity of the particles was estimated by assuming a mass-to-light ratio of $M/L = 4$.

using the so called Nuker profile (Lauer et al., 1995):

$$\mu(r) = 2^{(\beta-\gamma)/\alpha}\mu_b \left(\frac{r_b}{r}\right)^{\gamma} \left[1 + \left(\frac{r}{r_b}\right)^{\alpha}\right]^{(\gamma-\beta)/\alpha}, \tag{4.5}$$

where r_b is once again the break radius, μ_b is the surface brightness at the break radius, β and γ are the logarithmic slopes of the power-laws inside and outside of the break radius respectively, and α is the sharpness of the transition between the two slopes.

We use the "Levenberg-Marquardt" algorithm to fit the aforementioned core-Sérsic and Nuker models to the surface brightness profiles that we have calculated. Figure 4.4 shows a comparison of the resulting fits for snapshot 3 (refer to table 4.3), while figures A.2 and A.3, located in the appendix, show the fits for every snapshot that contains SMBH binaries. The values of the best-fit parameters are written on the figures, and looking at them, it is clear that the exact value of the best-fit break radius, i.e. the core radius estimate, depends quite heavily on the model used.
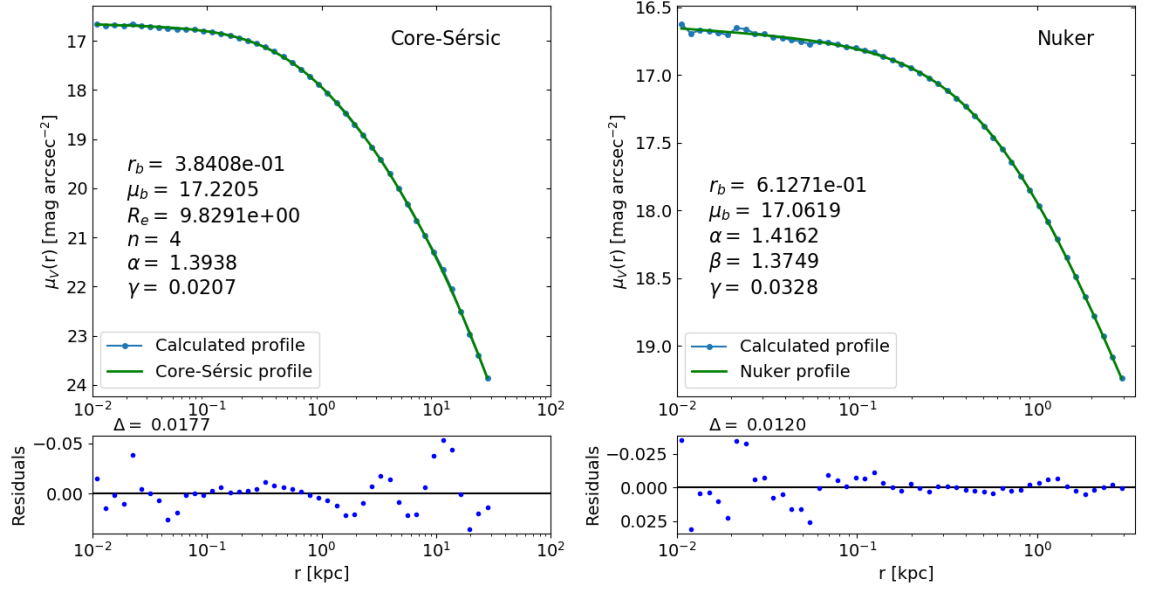
Figure 4.4: Core-Sérsic and Nuker profile fits of surface brightness profiles calculated from Snapshot 3 (top-left and top-right figures). The best fit parameters are written on the figures, and are in the same units as the axes (i.e. r_b and R_e in kilo-parsecs, and μ_b in V-band magnitudes per arc-second squared). The relative residuals of the fits are plotted under their respective figures. The delta describes the root-mean-square of the residuals.

Which model is better for estimating the size of the core is up for debate (Lauer et al., 2007b; Dullo and Graham, 2012). While the rms of the relative residuals seems to be consistently marginally smaller for the Nuker model when compared to the rms for the core-Sérsic model (compare figures A.2 and A.3), one also has to take into account that in the Nuker model the best-fit value for r_b is highly dependent on the fitting range (Graham et al., 2003b). Furthermore, as stated by Rantala et al. (2018), in order to get sensible values for all of the model parameters, the fitting range of the Nuker model has to be narrowed down closer to the galactic core ($\alpha \lesssim 1$ might prevent the model from describing the profile as a combination of two power-laws).

One could also estimate the size of the core without model fitting by using the so-called "cusp radius" r_γ, which is the radius at which the negative logarithmic slope of the surface brightness density γ' equals 1/2 (Carollo et al., 1997; Lauer

et al., 2007a). The cusp radius r_γ is also an estimation for the location where the inner power-law of the profile changes into the outer power-law, and thus equates to the core radius.

We calculate r_γ for all of the snapshots with SMBH binaries by calculating the first derivative (gradient) of the surface brightness profiles, and then using a "Nelder-Mead" minimization algorithm to find the radius, at which the gradient gets the value $-1/2$.

Figure 4.5 compares the core radius estimates from each of the three methods for every merger remnant from the snapshots. The break radii from the Nuker fits are consistently larger than the other core radius estimates, while also being the ones that, in general, agree least with the other values. However, a clear trend of the size of the core growing with the merger progenitors' central SMBH masses can be seen.

4.4 Velocity Anisotropy

One way of adding to the evidence that a galaxy has formed a core through core scouring by binary black holes, is to study its velocity anisotropy profile defined in Binney and Tremaine (2008):

$$\beta(r) = 1 - \frac{\sigma_\theta^2 - \sigma_\phi^2}{2\sigma_r^2} = 1 - \frac{\sigma_t^2}{\sigma_r^2}, \tag{4.6}$$

where σ_θ, σ_ϕ and σ_r are velocity dispersions in the spherical coordinates, and $\sigma_t = \sqrt{(\sigma_\theta^2 + \sigma_\phi^2)/2}$ is the tangential velocity dispersion. The β parameter describes the relation between objects in radial and tangential orbits around the black hole binary, where a negative β shows an abundance of tangential orbits, and positive an abundance of radial orbits.

Figure 4.6 shows β-profiles calculated from all of the merger remnant snapshots using equation 4.6. According to the profiles, the outer areas of the remnants are
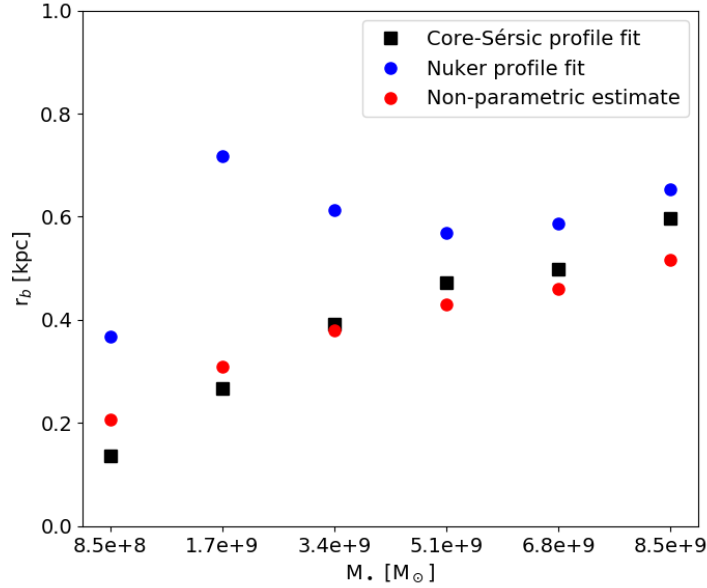
Figure 4.5: Comparison of core radii of the merger remnants, gained through three different methods: Core-Sérsic profile fitting (black squares), Nuker profile fitting (blue circles) and finding the "cusp radius" (red circles). The x-axis shows the masses of the central SMBHs of the merger progenitors.

dominated by radial orbits, while the majority of orbits near the centre are more tangential.

As the merging of two galaxies would cause a randomization of the stellar orbits, an area with negative β in the merger remnant, would imply that the stars on radial orbits have been ejected from the system. It has been shown that hardening black hole binaries can eject stars on highly radial orbits from the galactic core, which can then cause the outer orbits to become more radial (Quinlan and Hernquist, 1997; Milosavljević and Merritt, 2001; Thomas et al., 2014).

This could certainly be the reason behind the shapes of the β profiles seen in figure 4.6. It is clear that the presence of the SMBHs has an effect on the profiles' shape, as not only is the profile for the merger without an SMBH binary the only one completely dominated by radial orbits, but larger the binary's masses result in
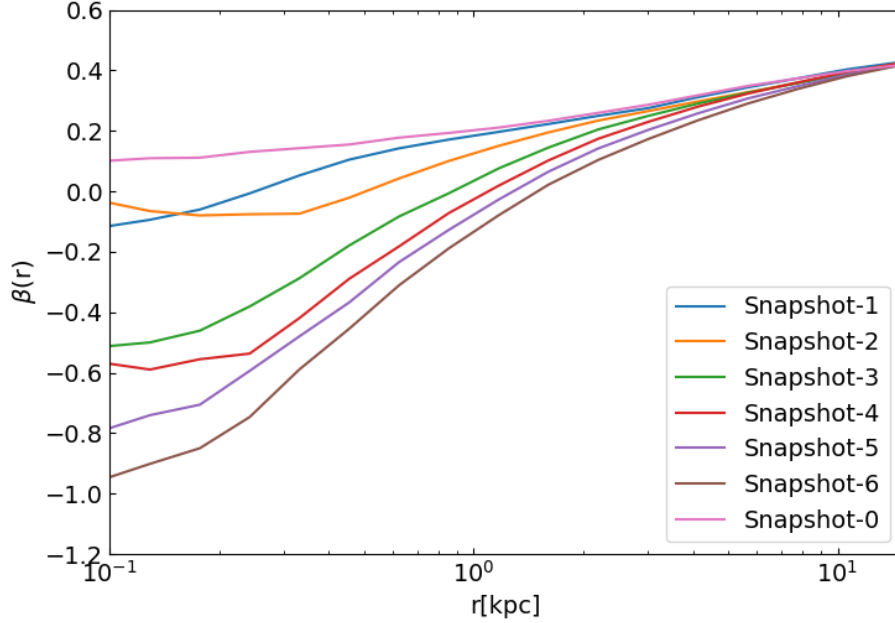
Figure 4.6: Velocity anisotropy (beta) profiles of the simulated merger remnants with central black holes.

a steeper slope in the profile. These effects also make sense in the context of ejection of stellar particles by black hole binaries. The larger the masses of the SMBHs in the binary are, the larger their gravitational sphere-of-influence is, and thus more the stellar particles with radial orbits can be ejected.

4.5   Line-of-Sight Kinematics

In order to make sure that the KETJU simulations produce results equivalent to observations, we analyse the line-of-sight (LOS) kinematics of the "snapshots". We will be analysing four different LOS velocity distribution properties: the average LOS velocity V_{avg}, the velocity dispersion σ, and the h_3 and h_4 parameters which correspond to the skewness and the kurtosis of the distribution respectively. The distribution from which these properties are calculated is defined as the following

modified Gaussian function (Rantala et al., 2018):

$$f(v) = I_0 e^{-\gamma^2/2}(1 + h_3 H_3(y) + h_4 H_4(y)), \tag{4.7}$$

where I_0 is a normalization constant, γ is the central slope of the particle density profile (maybe?), $y = (v - V_{\text{avg}})/\sigma$, and H_3 and H_4 are the third and fourth order Hermite polynomials respectively:

$$H_3(y) = \left(2\sqrt{2}y^3 - 3\sqrt{2}y\right)/\sqrt{6}, \tag{4.8}$$

$$H_4(y) = \left(4y^4 - 12y^2 + 3\right)/\sqrt{24}. \tag{4.9}$$

In order to calculate the above properties, we define the "line-of-sight" as the intermediate axis of the merger remnants, and orient the remnant accordingly using the inertia tensor. ... *Add text about inertia tensor, histogram forming, voronoi tessellation (Cappellari and Copin, 2003).* Figure 4.7 shows the voronoi binned 2D maps of the four LOS velocity distribution parameters for snapshot-0 and snapshot-6. Similar maps for all of the merger remnant snapshots are in figures A.4 and A.5 in the appendix.

Informative IFU map analysis

Another informative parameter that the 2D kinematic maps allow us to analyse is λ_R, which describes the angular momentum of the galaxy, and as such allows us to differentiate between slowly and fast rotating galaxies (Emsellem et al., 2007). The λ_R parameter is defined in a general form as:

$$\lambda_R \equiv \frac{\langle R|V|\rangle}{\langle R\sqrt{V^2 + \sigma^2}\rangle}, \tag{4.10}$$

where R the distance from the galactic centre, V is velocity, σ is the velocity dispersion, and $\langle\ \rangle$ denote that the nominator and denominator of the equation are velocity weighted means. However as most of the observational kinematic analysis of galaxies is done through binned 2D spectroscopy, and as the figures made from the kinematic results of our simulations try to mimic the ones gained through
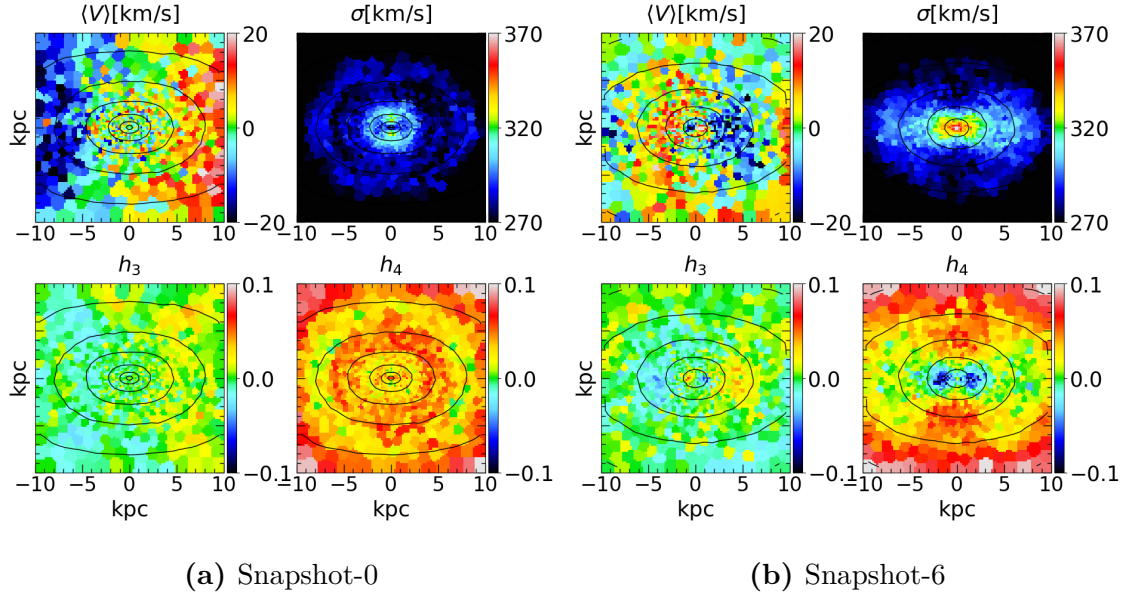
(a) Snapshot-0

(b) Snapshot-6

Figure 4.7: IFU-maps of average LOS-velocities, velocity dispersion, h_3 parameters and h_4 parameters from two simulated merger remnants. The four maps on the left are from a merger simulation where the progenitor galaxies had no central SMBHs, where as the four on the right are from a simulation with progenitor galaxies containing $M_\bullet = 8.5 \times 10^9 M_\odot$ central black holes.

observations, we will be using the following version of equation 4.10:

$$\lambda_R = \frac{\sum_{i=1}^{N_p} F_i R_i |V_i|}{\sum_{i=1}^{N_p} F_i R_i \sqrt{V_i^2 + \sigma_i^2}}, \qquad (4.11)$$

where F_i, R_i, V_i and σ_i are the flux, distance from the centre, velocity and velocity dispersion of the ith bin, and N_p is the number of bins. In the case of our simulations the bins are the voronoi bins described earlier in this section.

As stated before, λ_R allows us to classify observed and simulated galaxies as either slow or fast rotators; where slow rotators are usually more massive and luminous than fast rotators, and contain more non regular kinematic structures (Emsellem et al., 2007), as can be seen in figure 4.10. Determining whether a galaxy is a fast or a slow rotator by using λ_R, is done by comparing the value the parameter in question gets at the effective radius to some threshold. The original threshold used for differentiating the two rotator types is: $\lambda_{Re} < 0.1$, where λ_{Re} is the λ_R parameter at the effective radius, and galaxies fulfilling the condition are

classified as slow rotators (Emsellem et al., 2007). Later revisions by Emsellem et al. (2011) and Cappellari (2016) define the threshold as being either $\lambda_{Re} < 0.31\sqrt{\epsilon}$ or $\lambda_{Re} < 0.08 + \epsilon/4$ for $\epsilon < 0.4$ respectively, and as such take into account the shape of the galaxy in the form of its projected ellipticity (ϵ). Through including the ellipticity in the threshold, the former revision accounts for increased anisotropy in the kinematics of flatter galaxies, while the latter improves on the former by reducing the risk of misidentifying round non regular slow rotators as fast rotators.

Since two of the aforementioned slow rotator thresholds require us to know the ellipticity of the galaxy, we calculate the simulated merger remnants' ellipticities before analysing their rotation. The ellipticity calculations are done using a method described in Zemp et al. (2011), which uses the shape tensor:

$$\mathbf{S} = \frac{\int_V \rho(\mathbf{r})\omega(\mathbf{r})\mathbf{r}\mathbf{r}^T \, dV}{\int_V \rho\mathbf{r} \, dV}, \tag{4.12}$$

where $\mathbf{r}$ is position from the galactic centre, $\rho(\mathbf{r})$ is the mass density, V is the volume of an enclosed ellipsoid with the elliptical radius r_{ell}, and where the weighting function $\omega(\mathbf{r}) = 1$. The eigenvalues of the shape tensor correspond to $a^2/3$, $b^2/3$ and $c^2/3$; where a, b and c are the semi-principal axes; and which can be used to calculate the ellipticity as $\epsilon = 1 - b/a$. *explain further*

We calculate the λ_{Re} and ϵ_e for every merger simulation snapshot, and plot them against each other alongside the previously mentioned slow rotator thresholds and observations from the ATLAS[3D]-survey (Cappellari et al., 2011). The resulting plot can be seen in figure 4.8. Regardless of the threshold used for differentiating between slow and fast rotators, the merger remnants from the simulations are nonetheless clearly classified as slow rotators.

Galaxy	$M_\star$	$M_\bullet$	R_e	μ_e	n	$\langle V_{\text{LOS}} \rangle$	σ_e	λ_e	ϵ_e
	$[\times 10^{11} M_\odot]$	$[\times 10^{10} M_\odot]$	[kpc]	[mag/arcsec^2]		[km/s]	[km/s]		
(1)	(2)	(3)	(4)	(5)	(6)	(7)	(8)	(9)	(10)
Snapshot-6	4.960	2×0.85	5.507	20.26	4	6.9	311	0.024	0.11
NGC 1600	5.0	1.7	~ 16	~ 22.8	5.83	3.4	293	0.026	032

Table 4.4: Comparison between the physical properties of the simulated merger remnant "Snapshot-6" and the galaxy NGC 1600. The properties described in the columns of the table are explained below, with the sources for the properties of NGC 1600 being written inside the brackets.

(1) Name of the galaxy.

(2) Total stellar mass (Thomas et al., 2016).

(3) Central black hole mass (Thomas et al., 2016).

(4) Effective radius (Thomas et al., 2016). For NGC 1600, the effective radius is changed from arc seconds to kpc by assuming that it is located at the distance of $D = 64$ Mpc (Thomas et al., 2016).

(5) Surface brightness at the effective radius. Calculated from the best fit core-Sérsic profile parameters given in Thomas et al. (2016).

(6) Sérsic index from the best fitting core-Sérsic profile fit (Thomas et al., 2016).

(7) Mean line-of-sight velocity inside the effective radius (Bender et al., 1994).

(8) Velocity dispersion inside the effective radius (Veale et al., 2017). For "Snapshot-6", the given velocity dispersion is calculated from a Voronoi binned image as the mean of the velocity dispersion values of the bins located inside the effective radius.

(9) Spin parameter at the effective radius (Veale et al., 2018).

(10) For "Snapshot-6": ellipticity of the galaxy at the effective radius; and for GC 1600: luminosity weighted ellipticity (Goullaud et al., 2018).
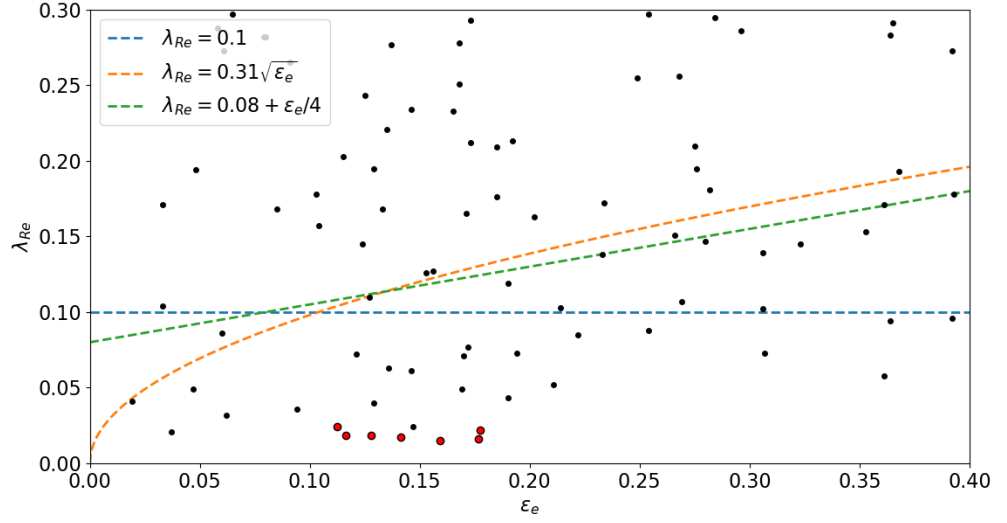
Figure 4.8: The values of the λ_{Re}-parameter of galaxies, plotted against their ellipticity at the effective radius. The red dots correspond to the simulated merger remnants, where as the black dots correspond to galaxies observed in the ATLAS[3D]-survey (Cappellari et al., 2011; Emsellem et al., 2011). The dashed lines display different slow rotator thresholds as a function of ellipticity (Emsellem et al., 2007, 2011; Cappellari, 2016).

4.6 Comparison to Observations

4.7 Implications
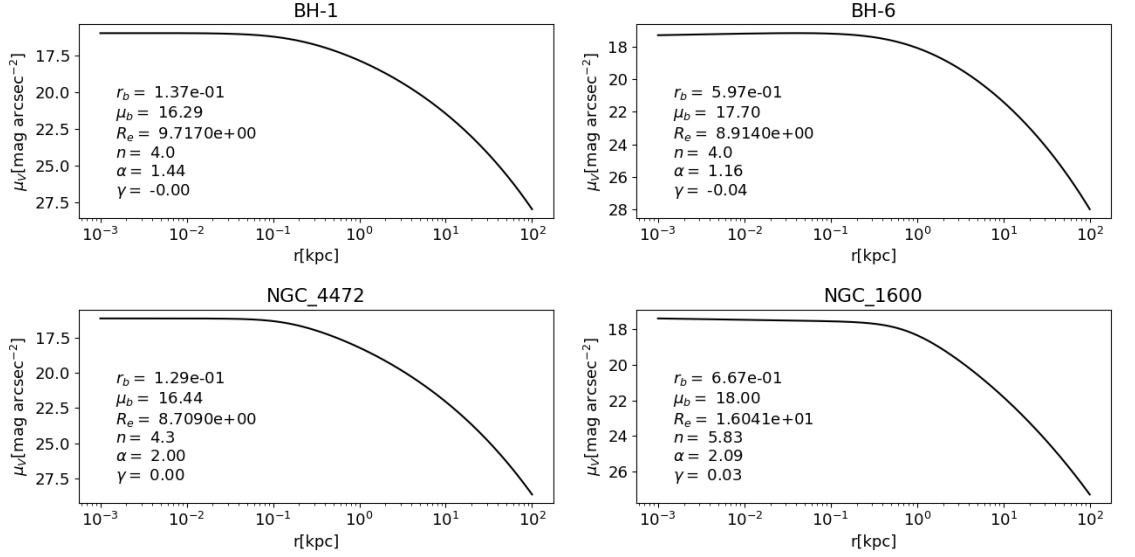
Figure 4.9: Core-Sérsic profile fits of surface brightness profiles calculated from either merger simulation results (top figures) or observed galaxies (bottom figures). The respective fit parameters are written on the figures in units that correspond to the axes. The progenitors of the top-left simulation contained $8.5 \times 10^8 M_\odot$ mass central SMBHs, and $8.5 \times 10^9 M_\odot$ mass central SMBHs in the top-right simulation. The parameters for NGC1600's profile (bottom right), are changed from the units used by Thomas et al. (2016) to the above by assuming $V - R = 0.5$ (the same assumption being done by Lauer et al. (2007b)), and by using the distance $D = 64$Mpc (Thomas et al., 2016) in order to define the relation between arc seconds and parsecs. As one can see, the profiles gained from simulations and observations are quite similar to each other.
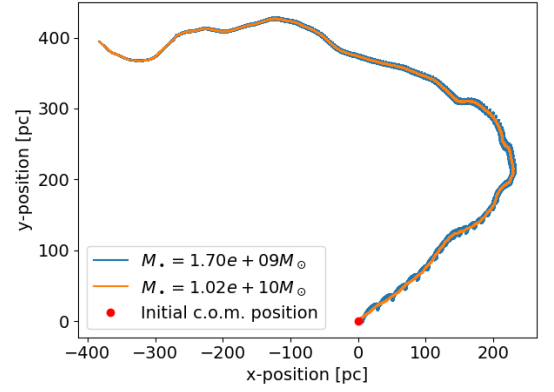
(a) NGC 3414

(b) NGC 4111
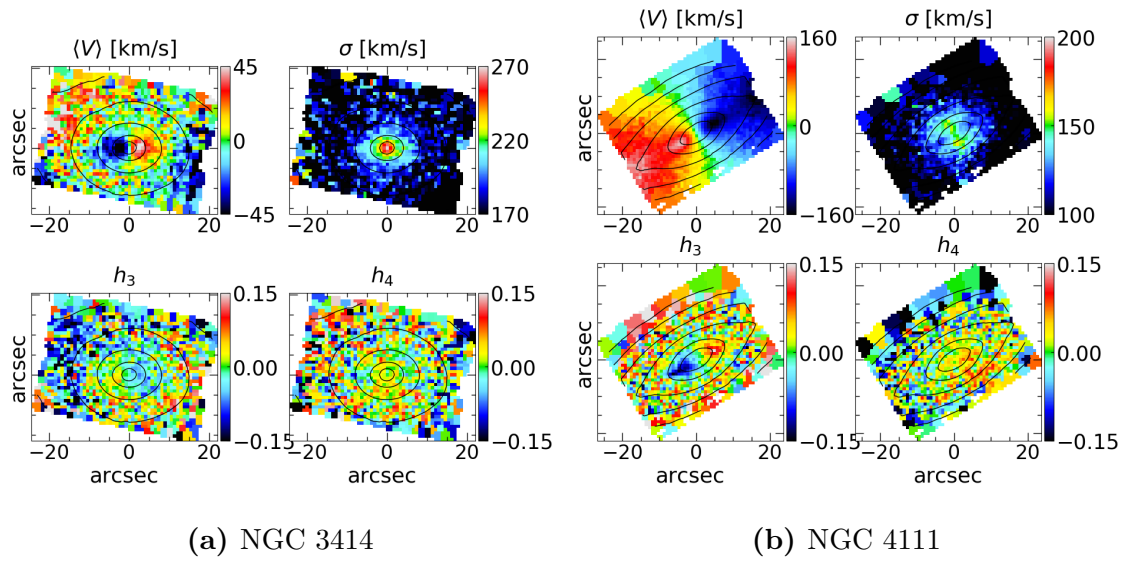
Figure 4.10: Comparison between the IFU-maps of known slow and fast rotator galaxies from the ATLAS^{3D} survey. The maps show the average LOS-velocities, velocity dispersion, h_3 parameters and h_4 parameters of NGC 3414 (Emsellem et al., 2004) and NGC 4111 (Cappellari et al., 2011).
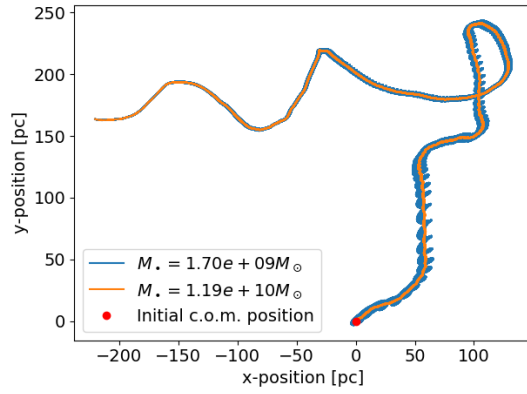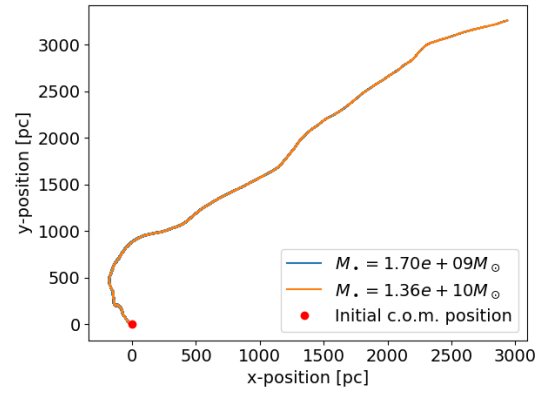
5. Conclusions

A. Figures
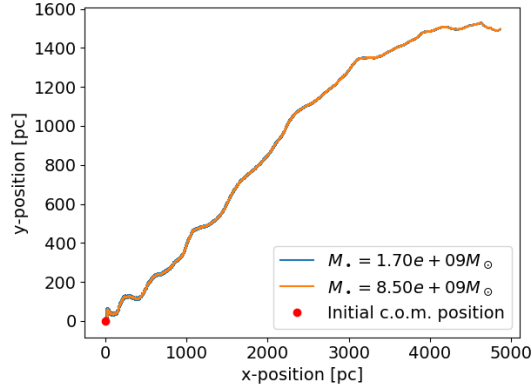
(a) Run 1

(b) Run 2

(c) Run 3

(d) Run 4

Figure A.1: The trajectories of the black holes from simulation runs by Mannerkoski et al. (2019). The coordinates are centred on the initial location of the centre-of-mass of the black hole system. The orange and blue lines show the paths taken by the smaller and larger black holes respectively during the simulation.
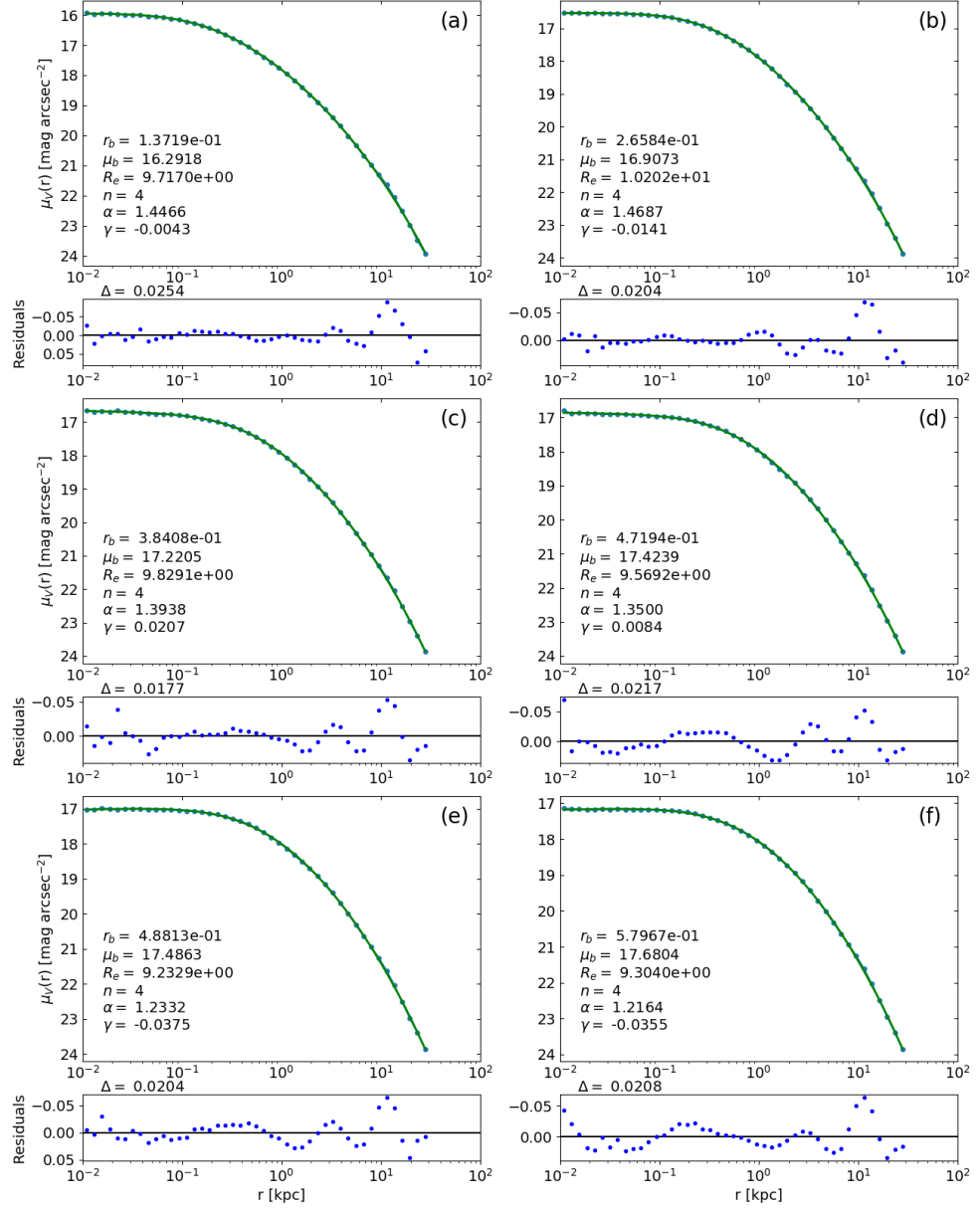
Figure A.2: Core-Sérsic profile fits of the surface brightness data calculated from all of the individual simulated merger remnants with progenitors containing central supermassive black holes. The letters (a)-(f) denote the different snapshots ((a): Snapshot-1, (b): Snapshot-2, (c): Snapshot-3, (d): Snapshot-4, (e): Snapshot-5, (f): Snapshot-6).
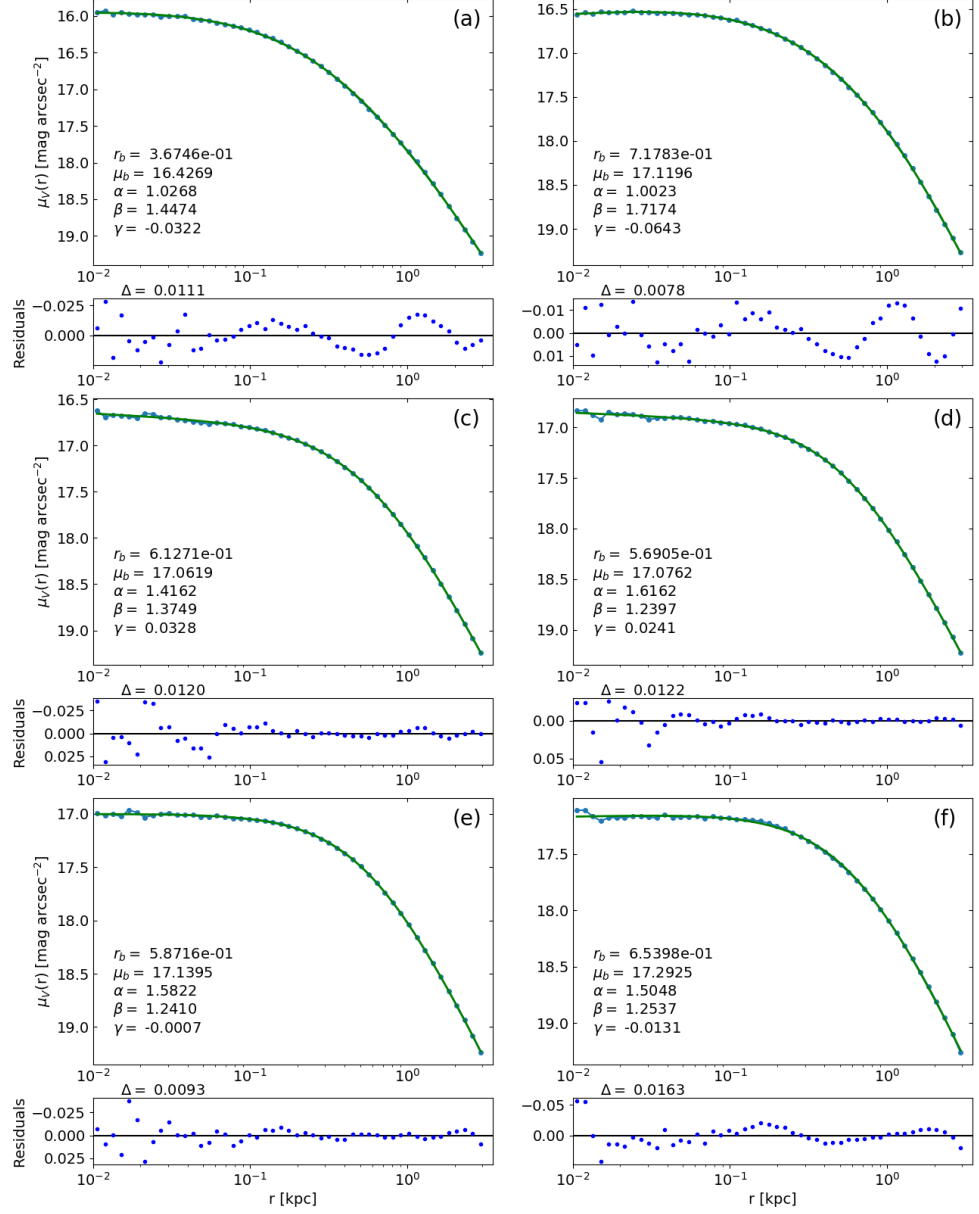
Figure A.3: Nuker profile fits of the surface brightness data calculated from all of the individual simulated merger remnants with progenitors containing central supermassive black holes. The letters (a)-(f) denote the different merger remnants ((a): Snapshot-1, (b): Snapshot-2, (c): Snapshot-3, (d): Snapshot-4, (e): Snapshot-5, (f): Snapshot-6).
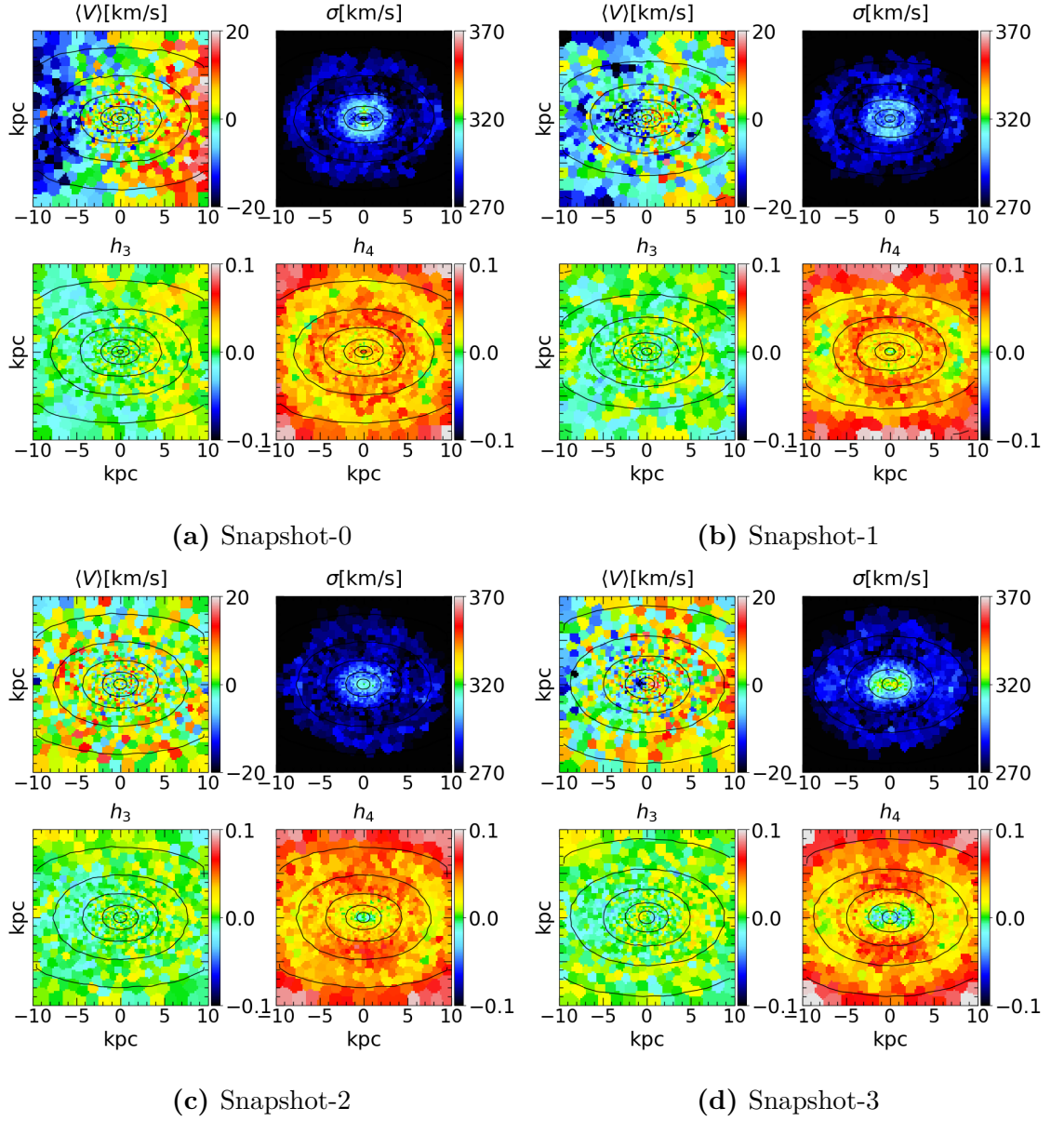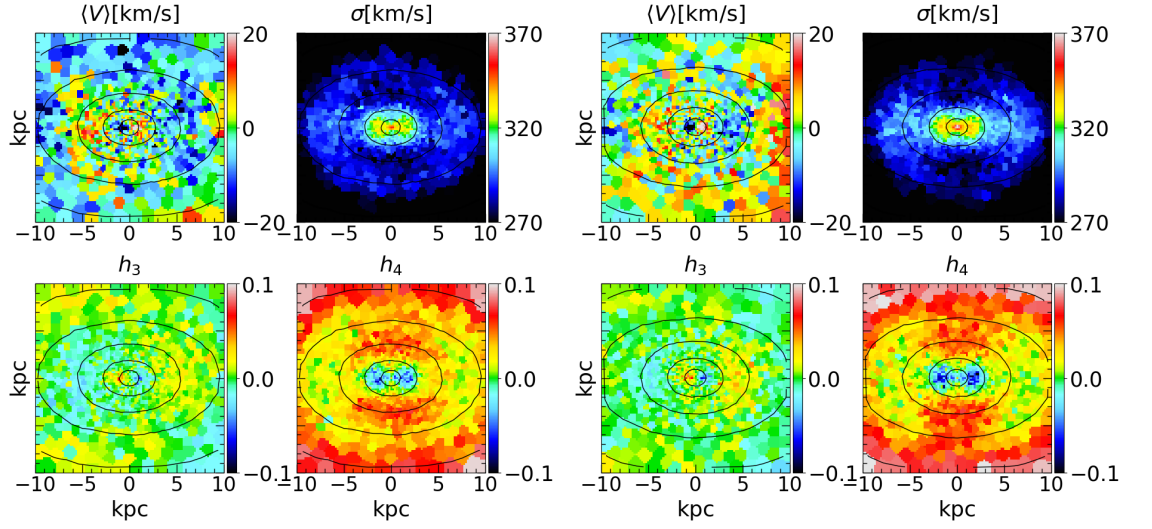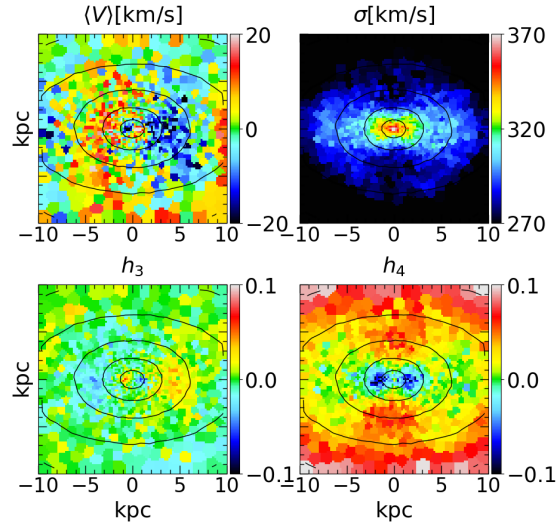
(a) Snapshot-0

(b) Snapshot-1

(c) Snapshot-2

(d) Snapshot-3

Figure A.4: IFU-maps of average LOS-velocities, velocity dispersion, h_3 parameters and h_4 parameters from four simulated merger remnants: Snapshot-0, Snapshot-1, Snapshot-2 and Snapshot-3.

(a) Snapshot-4

(b) Snapshot-5

(c) Snapshot-6

Figure A.5: IFU-maps of average LOS-velocities, velocity dispersion, h_3 parameters and h_4 parameters from three simulated merger remnants: Snapshot-4, Snapshot-5 and Snapshot-6.

Bibliography

R. Bender, R. P. Saglia, and O. E. Gerhard. Line-of-sight velocity distributions of elliptical galaxies. *Monthly Notices of the Royal Astronomical Society*, 269: 785–813, Aug 1994. doi: 10.1093/mnras/269.3.785.

James Binney and Scott Tremaine. *Galactic Dynamics: Second Edition.* 2008.

M. Cappellari, E. Emsellem, D. Krajnović, R. M. McDermid, N. Scott, G. A. Verdoes Kleijn, L. M. Young, K. Alatalo, R. Bacon, L. Blitz, M. Bois, F. Bournaud, M. Bureau, R. L. Davies, T. A. Davis, P. T. de Zeeuw, P.-A. Duc, S. Khochfar, H. Kuntschner, P.-Y. Lablanche, R. Morganti, T. Naab, T. Oosterloo, M. Sarzi, P. Serra, and A.-M. Weijmans. The ATLAS^{3D} project - I. A volume-limited sample of 260 nearby early-type galaxies: science goals and selection criteria. *Monthly Notices of the Royal Astronomical Society*, 413:813–836, May 2011. doi: 10.1111/j.1365-2966.2010.18174.x.

Michele Cappellari. Structure and Kinematics of Early-Type Galaxies from Integral Field Spectroscopy. *Annual Review of Astronomy and Astrophysics*, 54:597–665, Sep 2016. doi: 10.1146/annurev-astro-082214-122432.

Michele Cappellari and Yannick Copin. Adaptive spatial binning of integral-field spectroscopic data using Voronoi tessellations. *Monthly Notices of the Royal Astronomical Society*, 342(2):345–354, Jun 2003. doi: 10.1046/j.1365-8711.2003. 06541.x.

C. Marcella Carollo, Marijn Franx, Garth D. Illingworth, and Duncan A. Forbes. Ellipticals with Kinematically Distinct Cores: V - I Color Images with WPFC2. *The Astrophysical Journal*, 481(2):710–734, May 1997. doi: 10.1086/304060.

W. Dehnen. A Family of Potential-Density Pairs for Spherical Galaxies and Bulges. *Monthly Notices of the Royal Astronomical Society*, 265:250, Nov 1993. doi: 10. 1093/mnras/265.1.250.

Bililign T. Dullo and Alister W. Graham. Sizing up Partially Depleted Galaxy Cores. *The Astrophysical Journal*, 755(2):163, August 2012. doi: 10.1088/0004-637X/ 755/2/163.

E. Emsellem, M. Cappellari, R. F. Peletier, R. M. McDermid, R. Bacon, M. Bureau, Y. Copin, R. L. Davies, D. Krajnović, H. Kuntschner, B. W. Miller, and P. T. de Zeeuw. The SAURON project - III. Integral-field absorption-line kinematics of 48 elliptical and lenticular galaxies. *Monthly Notices of the Royal Astronomical Society*, 352:721–743, August 2004. doi: 10.1111/j.1365-2966.2004.07948.x.

E. Emsellem, M. Cappellari, D. Krajnović, K. Alatalo, L. Blitz, M. Bois, F. Bournaud, M. Bureau, R. L. Davies, T. A. Davis, P. T. de Zeeuw, S. Khochfar, H. Kuntschner, P.-Y. Lablanche, R. M. McDermid, R. Morganti, T. Naab, T. Oosterloo, M. Sarzi, N. Scott, P. Serra, G. van de Ven, A.-M. Weijmans, and L. M. Young. The ATLAS^{3D} project - III. A census of the stellar angular momentum within the effective radius of early-type galaxies: unveiling the distribution of fast and slow rotators. *Monthly Notices of the Royal Astronomical Society*, 414:888–912, June 2011. doi: 10.1111/j.1365-2966.2011.18496.x.

Eric Emsellem, Michele Cappellari, Davor Krajnović, Glenn van de Ven, R. Bacon, M. Bureau, Roger L. Davies, P. T. de Zeeuw, Jesús Falcón-Barroso, Harald Kuntschner, Richard McDermid, Reynier F. Peletier, and Marc Sarzi. The

SAURON project - IX. A kinematic classification for early-type galaxies. *Monthly Notices of the Royal Astronomical Society*, 379(2):401–417, Aug 2007. doi: 10.1111/j.1365-2966.2007.11752.x.

Charles F. Goullaud, Joseph B. Jensen, John P. Blakeslee, Chung-Pei Ma, Jenny E. Greene, and Jens Thomas. The MASSIVE Survey. IX. Photometric Analysis of 35 High-mass Early-type Galaxies with HST WFC3/IR. *The Astrophysical Journal*, 856(1):11, March 2018. doi: 10.3847/1538-4357/aab1f3.

Alister W. Graham, Peter Erwin, I. Trujillo, and A. Asensio Ramos. A New Empirical Model for the Structural Analysis of Early-Type Galaxies, and A Critical Review of the Nuker Model. *The Astronomical Journal*, 125(6):2951–2963, Jun 2003a. doi: 10.1086/375320.

Alister W. Graham, Peter Erwin, I. Trujillo, and A. Asensio Ramos. A New Empirical Model for the Structural Analysis of Early-Type Galaxies, and A Critical Review of the Nuker Model. *The Astronomical Journal*, 125(6):2951–2963, Jun 2003b. doi: 10.1086/375320.

T. R. Lauer, E. A. Ajhar, Y. I. Byun, A. Dressler, S. M. Faber, C. Grillmair, J. Kormendy, D. Richstone, and S. Tremaine. The Centers of Early-Type Galaxies with HST.I.An Observational Survey. *The Astronomical Journal*, 110:2622, Dec 1995. doi: 10.1086/117719.

Tod R. Lauer, S. M. Faber, Douglas Richstone, Karl Gebhardt, Scott Tremaine, Marc Postman, Alan Dressler, M. C. Aller, Alexei V. Filippenko, and Richard Green. The Masses of Nuclear Black Holes in Luminous Elliptical Galaxies and Implications for the Space Density of the Most Massive Black Holes. *The Astrophysical Journal*, 662(2):808–834, Jun 2007a. doi: 10.1086/518223.

Tod R. Lauer, Karl Gebhardt, S. M. Faber, Douglas Richstone, Scott Tremaine, John

Kormendy, M. C. Aller, Ralf Bender, Alan Dressler, and Alexei V. Filippenko. The Centers of Early-Type Galaxies with Hubble Space Telescope. VI. Bimodal Central Surface Brightness Profiles. *The Astrophysical Journal*, 664(1):226–256, July 2007b. doi: 10.1086/519229.

Matias Mannerkoski, Peter H. Johansson, Pauli Pihajoki, Antti Rantala, and Naab Thorsten. Inspiral of Supermassive Black Holes In Galactic Scale Simulations. *Monthly Notices of the Royal Astronomical Society*, 856(1):11, ? 2019. doi: 10. 3847/1538-4357/aab1f3.

Miloš Milosavljević and David Merritt. Formation of Galactic Nuclei. *The Astrophysical Journal*, 563(1):34–62, Dec 2001. doi: 10.1086/323830.

Gerald D. Quinlan and Lars Hernquist. The dynamical evolution of massive black hole binaries — II. Self-consistent N-body integrations. *New Astronomy*, 2(6): 533–554, Dec 1997. doi: 10.1016/S1384-1076(97)00039-0.

Antti Rantala, Peter H. Johansson, Thorsten Naab, Jens Thomas, and Matteo Frigo. The Formation of Extremely Diffuse Galaxy Cores by Merging Supermassive Black Holes. *The Astrophysical Journal*, 864(2):113, September 2018. doi: 10.3847/ 1538-4357/aada47.

J. Thomas, R. P. Saglia, R. Bender, P. Erwin, and M. Fabricius. The Dynamical Fingerprint of Core Scouring in Massive Elliptical Galaxies. *The Astrophysical Journal*, 782(1):39, Feb 2014. doi: 10.1088/0004-637X/782/1/39.

Jens Thomas, Chung-Pei Ma, Nicholas J. McConnell, Jenny E. Greene, John P. Blakeslee, and Ryan Janish. A 17-billion-solar-mass black hole in a group galaxy with a diffuse core. *Nature*, 532(7599):340–342, April 2016. doi: 10.1038/ nature17197.

Melanie Veale, Chung-Pei Ma, Jens Thomas, Jenny E. Greene, Nicholas J. Mc-
Connell, Jonelle Walsh, Jennifer Ito, John P. Blakeslee, and Ryan Janish. The
MASSIVE Survey - V. Spatially resolved stellar angular momentum, velocity dis-
persion, and higher moments of the 41 most massive local early-type galaxies.
Monthly Notices of the Royal Astronomical Society, 464(1):356–384, January 2017.
doi: 10.1093/mnras/stw2330.

Melanie Veale, Chung-Pei Ma, Jenny E. Greene, Jens Thomas, John P. Blakeslee,
Jonelle L. Walsh, and Jennifer Ito. The MASSIVE survey - VIII. Stellar velocity
dispersion profiles and environmental dependence of early-type galaxies. *Monthly
Notices of the Royal Astronomical Society*, 473(4):5446–5467, February 2018. doi:
10.1093/mnras/stx2717.

Marcel Zemp, Oleg Y. Gnedin, Nickolay Y. Gnedin, and Andrey V. Kravtsov. On
Determining the Shape of Matter Distributions. *The Astrophysical Journal Sup-
plement*, 197(2):30, December 2011. doi: 10.1088/0067-0049/197/2/30.